

# IRAM 30 m CO-line Observation toward PeVatron Candidate G106.3+2.7: Direct Interaction between the Shock and the Molecular Cloud Remains Uncertain

QIAN-CHENG LIU<sup>1</sup>, PING ZHOU<sup>1,2</sup>, YANG CHEN<sup>1,2</sup>

<sup>1</sup>*Department of Astronomy, Nanjing University, 163 Xianlin Avenue, Nanjing 210023, People's Republic of China; ygchen@nju.edu.cn, pingzhou@nju.edu.cn*

<sup>2</sup>*Key Laboratory of Modern Astronomy and Astrophysics, Nanjing University, Ministry of Education, Nanjing 210093, People's Republic of China*

## ABSTRACT

Supernova remnant (SNR) G106.3+2.7 was recently found to be one of the few potential Galactic hadronic PeVatrons. Aiming to test how solid the SNR is associated with the molecular clouds (MCs) that are thought to be responsible for hadronic interaction, we performed a new CO observation with the IRAM 30 m telescope toward its “belly” region, which is coincident with the centroid of the  $\gamma$ -ray emission. There is a filament structure in the local-standard-of-rest velocity interval  $-8$  to  $-5$  km s<sup>-1</sup> that nicely follows the northern radio boundary of the SNR. We have seen asymmetric broad profiles of <sup>12</sup>CO lines, with widths of a few km s<sup>-1</sup>, along the northern boundary and in the “belly” region of G106.3+2.7, but similar <sup>12</sup>CO line profiles are also found outside the SNR boundary. Further, the low <sup>12</sup>CO  $J=2-1/J=1-0$  line ratios suggest the MCs are cool. Therefore, it is still uncertain whether the MCs are directly disturbed by the SNR shocks, but we do find some clues that the MCs are nearby and thus can still be illuminated by the escaped protons from the SNR. Notably, we find an expanding molecular structure with a velocity of  $\sim 3.5$  km s<sup>-1</sup> and a velocity gradient of the MCs across the SNR from  $\sim -3$  to  $-7$  km s<sup>-1</sup>, which could be explained as the effect of the wind blown by the SNR’s progenitor star.

*Keywords:* ISM: individual objects (G106.3+2.7) – ISM: supernova remnants – ISM: molecular clouds

## 1. INTRODUCTION

Supernova remnants (SNRs) are suggested to be one of the major factories to produce cosmic rays (CRs) up to  $\sim 10^{15}$  eV. High-energy GeV/TeV  $\gamma$ -ray photons can be produced via either the interaction between the CR protons and the gas material (hadronic origin) or inverse-Compton scattering of relativistic electrons (leptonic origin). The former scenario requires a dense environmental medium, such as molecular clouds (MCs), while the latter origin

is not subject to the nearby density. Therefore, an investigation of the molecular environment of an  $\gamma$ -ray-emitting SNR is vital to distinguish the origin of the high-energy emission.

SNR G106.3+2.7 has attracted substantial attention recently, as it was found to be one of the few potential Galactic hadronic PeVatrons (Albert et al. 2020; Tibet AS $\gamma$  Collaboration 2021; Cao et al. 2021). Extended  $\gamma$ -ray emission has been detected with Fermi-LAT (Xin et al. 2019), Milagro (Abdo et al. 2007), VERITAS

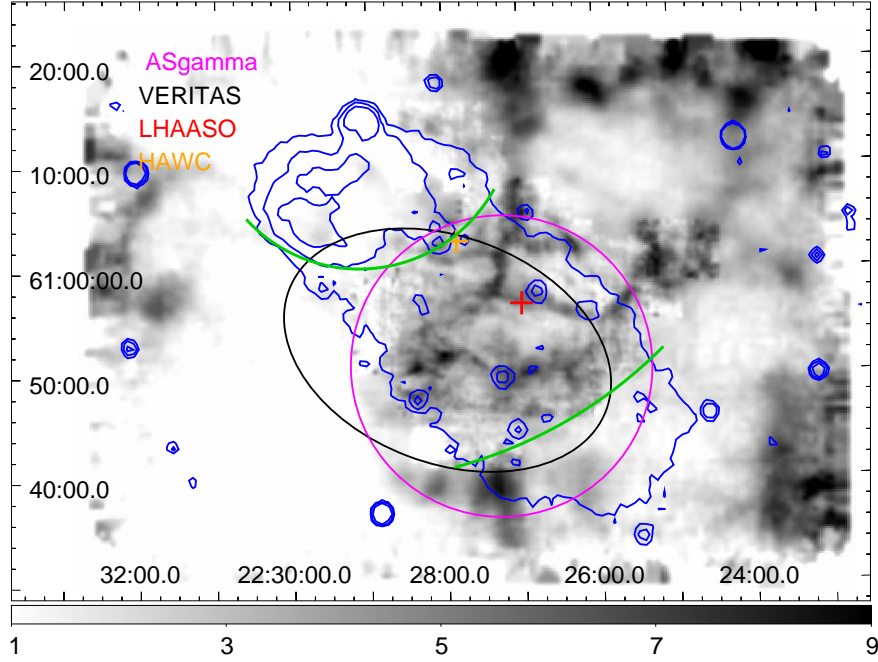


**Figure 1.**  $^{12}\text{CO}$   $J=1-0$  intensity map integrated in velocity range  $-10$  to  $-2\text{ km s}^{-1}$ , overlaid by 1.4 GHz radio contours from the CGPS (Taylor et al. 2003) in levels 6.9, 7.3, and 8 K. The magenta circle and black ellipse represent the gamma-ray emission detected by the Tibet AS $\gamma$  (Tibet AS $\gamma$  Collaboration 2021) and VERITAS (Acciari et al. 2009), respectively. The red and orange crosses show the best-fit positions of the LHAASO (Cao et al. 2021) and HAWC (Albert et al. 2020) sources. The green arcs crudely separate the “head”, “belly”, and “tail” regions (referring to the upper, middle, and lower parts, respectively) of the SNR described in this paper. The upper arc is adopted from Ge et al. (2021), and the lower arc follows the southwestern edge of the field of view of our IRAM observation.

(Acciari et al. 2009), and the Tibet AS $\gamma$  experiment (Tibet AS $\gamma$  Collaboration 2021) from G106.3+2.7 (see Figure 1). Recently, nonthermal X-ray emission was also discovered based on the analysis of *Chandra*, *XMM-Newton* and *Suzaku* data (Ge et al. 2021; Fujita et al. 2021). There is a bright X-ray point source toward the radio peak of G106.3+2.7 (Halpern et al. 2001b), and it was later confirmed to be a pulsar in the radio, X-rays (Halpern et al. 2001a), and the  $\gamma$ -ray (Abdo et al. 2009) bands. The existence of a pulsar establishes the core-collapse origin of G106.3+2.7.

G106.3+2.7 has a comet-shaped morphology in the radio band, with a bright head in the northeast and a tail toward the southwest (Pineault & Joncas 2000). It was suggested to be located at the edge of a large HI bub-

ble and associated with the MCs at a systemic local-standard-of-rest (LSR) velocity of about  $-6\text{ km s}^{-1}$  based mainly on the spatial correspondence (Kothes et al. 2001). This HI bubble was suggested to be created by stellar winds and SNe in the previous generation. Furthermore, the head of the SNR is found to be located in a small HI bubble (Kothes et al. 2001). Spatial coincidence has also been used to indicate a possible association between the  $\gamma$ -ray emission, the SNR, and the MCs (e.g., Acciari et al. 2009; Xin et al. 2019; Tibet AS $\gamma$  Collaboration 2021; Bao & Chen 2021). However, the nature of the  $\gamma$ -ray emission (hadronic or leptonic origin) is still under debate (e.g., Acciari et al. 2009; Xin et al. 2019; Albert et al. 2020; Liu et al. 2020b), and there is little dedicated investigation that aims at kinematically clarifying if the

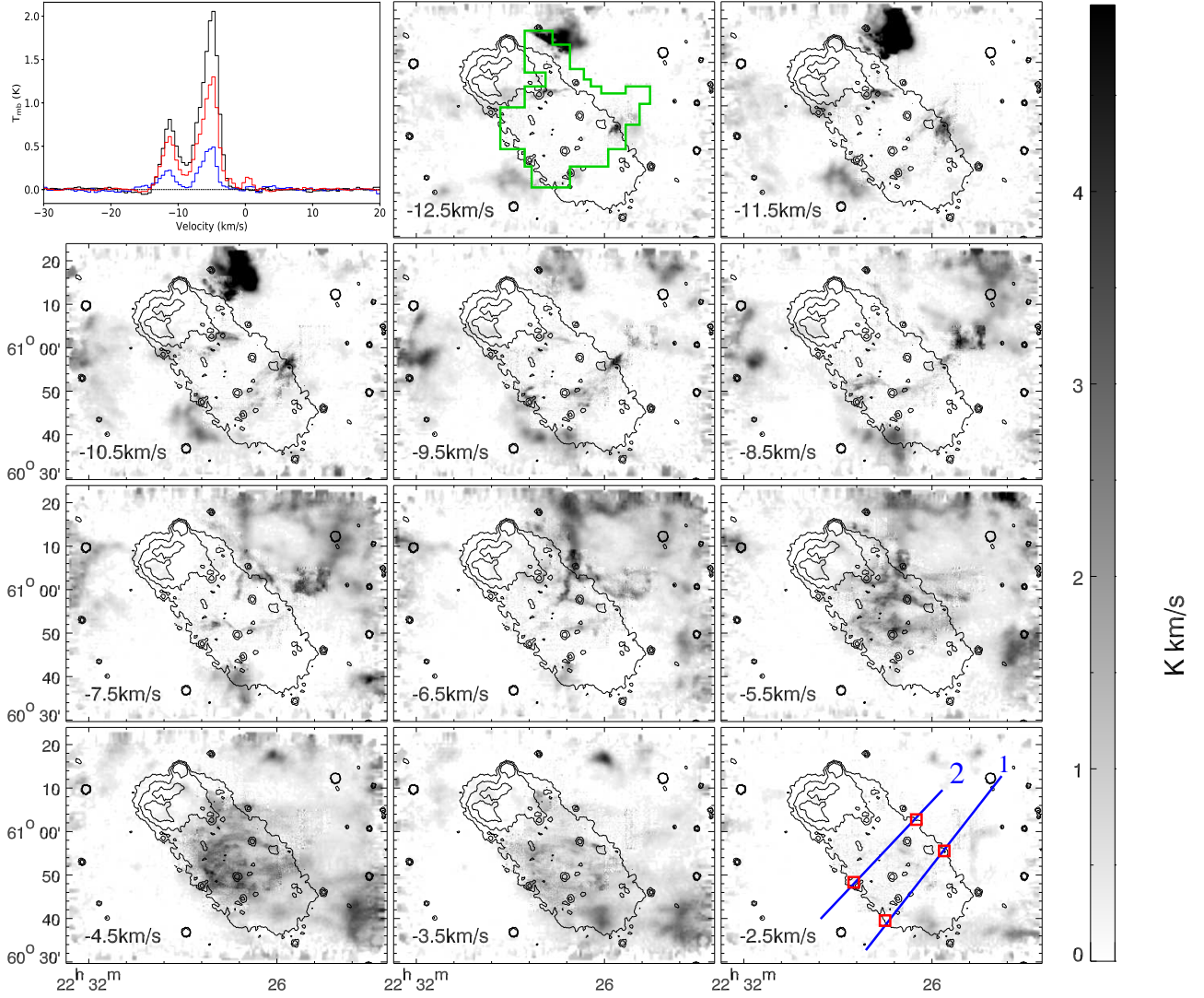


**Figure 2.**  $^{12}\text{CO } J=1-0$  intensity map integrated at  $1\text{ km s}^{-1}$  in the velocity range  $-13$  to  $-2\text{ km s}^{-1}$ , overlaid by radio contours the same as those in Figure 1. The region enclosed with the green polygon in the top middle panel delineates the region we observed with the IRAM 30 m telescope, and the data within this region for all the panels are from IRAM 30 m telescope. The data outside this region are from the archived PMOD. The data from the IRAM 30 m telescope have been resampled and re-grid to match the velocity resolution and pixel size of the PMOD data, and the data from PMOD has been multiplied by a factor of 2 for better visibility. The top left panel shows the averaged CO spectra of the polygon region in the velocity range  $-30$  to  $20\text{ km s}^{-1}$  from the IRAM observation. The black line is for  $^{12}\text{CO } J=1-0$ , the red line is for  $^{12}\text{CO } J=2-1$ , the blue line is for  $^{13}\text{CO } J=1-0$ , and the dashed line is for the 0 K main-beam temperature. The  $^{13}\text{CO } J=1-0$  line has been multiplied by a factor of three for better visibility. The lines used to make the position-velocity diagrams in Figure 3 are indicated in the bottom right panel in dark blue.

MCs are directly disturbed by the SNR shock (e.g., asymmetric broad-line profiles of  $^{12}\text{CO}$  lines, high  $^{12}\text{CO } J=2-1/J=1-0$  line ratios, etc.; Jiang et al. 2010; Chen et al. 2014). A new, independent CO observation with higher spatial and velocity resolution is therefore needed, which helps explore the astrophysical environment toward the direction of G106.3+2.7.

Here, we present a new CO-line observation using the IRAM 30 m telescope toward G106.3+2.7 and search for kinematic and physical signatures of the SNR-MC interaction. The observation and the data reduction process are described in Section 2, and the results are presented in Section 3; the discussion of the main results and the summary are presented in Section 4 and 5, respectively.

## 2. OBSERVATION AND DATA REDUCTION

Our observations of molecular lines toward G106.3+2.7 was made simultaneously in  $^{12}\text{CO } J=1-0$ ,  $^{12}\text{CO } J=2-1$ , and  $^{13}\text{CO } J=1-0$  with the IRAM 30 m telescope during 2020 December, 22 – 30, for a total of 40 hr. The observations covered an irregular polygon region toward the “belly” region of G106.3+2.7 with an area of about  $680 \text{ arcmin}^2$  (see the top middle panel of Figure 2). The mapping was conducted with the on-the-fly position-switching mode, using the Eight Mixer Receiver in E0 and E1 band and the fast Fourier transform spectrometers (FTS). The backend FTS provided a bandwidth of 16 GHz and a spectral resolution of 200 kHz. The velocity resolution is thus  $\sim 0.5 \text{ km s}^{-1}$  for  $^{12}\text{CO } J=1-0$  and  $^{13}\text{CO } J=1-0$ , and  $\sim 0.25 \text{ km s}^{-1}$  for  $^{12}\text{CO } J=2-1$ . The half-power beamwidth (HPBW) of the telescope is about  $21''$  at 115 GHz and about  $10''.7$  at 230 GHz, and the main-beam efficiency is about 0.78 at 115 GHz and about 0.59 at 230 GHz. To better study the three CO transitions, we have convolved the angular resolution to  $22''$  and resampled the velocity resolution to  $0.5 \text{ km s}^{-1}$  for

all line data. The rms noise levels of the main-beam temperature ( $T_{\text{mb}}$ ) of the convolved and resampled data are  $\sim 0.07 - 0.2 \text{ K}$  for  $^{13}\text{CO } J=1-0$  lines,  $\sim 0.2 - 0.8 \text{ K}$  for  $^{12}\text{CO } J=1-0$  lines, and  $\sim 0.06 - 0.2 \text{ K}$  for  $^{12}\text{CO } J=2-1$  lines. All the IRAM 30 m data were reduced with the GILDAS/CLASS package developed by the IRAM observatory <sup>1</sup>.

To study the larger-scale environment of the SNR, we have used the archived  $^{12}\text{CO } J=1-0$  data obtained with the 13.7 m millimeter-wavelength telescope of the Purple Mountain Observatory at Delingha (PMOD). The HPBW of the data is about  $50''$ , and the velocity resolution of the data is about  $0.16 \text{ km s}^{-1}$ . The rms noise level of the data varies in a range of  $\sim 0.1 - 0.2 \text{ K}$ . We also used 1.4 GHz radio continuum emission data from the Canadian Galactic Plane Survey (CGPS; Taylor et al. 2003).

## 3. RESULTS

### 3.1. Spatial Distribution of the Molecular Clouds

The top left panel of Figure 2 shows the  $^{12}\text{CO } J=1-0$ ,  $^{12}\text{CO } J=2-1$ , and  $^{13}\text{CO } J=1-0$  spectra averaged from the polygon region that was observed with the IRAM 30 m telescope. There are two prominent CO emission peaks, at around  $-11 \text{ km s}^{-1}$  and  $-4.5 \text{ km s}^{-1}$ . To examine the spatial distribution of these MCs, we have made  $^{12}\text{CO } J=1-0$  emission channel maps in the velocity range  $-13 \text{ km s}^{-1}$  to  $-2 \text{ km s}^{-1}$  using the highest spatial resolution CO data to date (Figure 2, where we have inserted the data from the IRAM 30 m telescope into the data from the PMOD). The maps cover the main components of the two emission peaks.

There are a few noticeable structures in this velocity range. (1) In velocity interval  $-8$  to  $-5 \text{ km s}^{-1}$ , except for the envelope around the head region of the SNR as noticed by

<sup>1</sup> <http://www.iram.fr/IRAMFR/GILDAS>

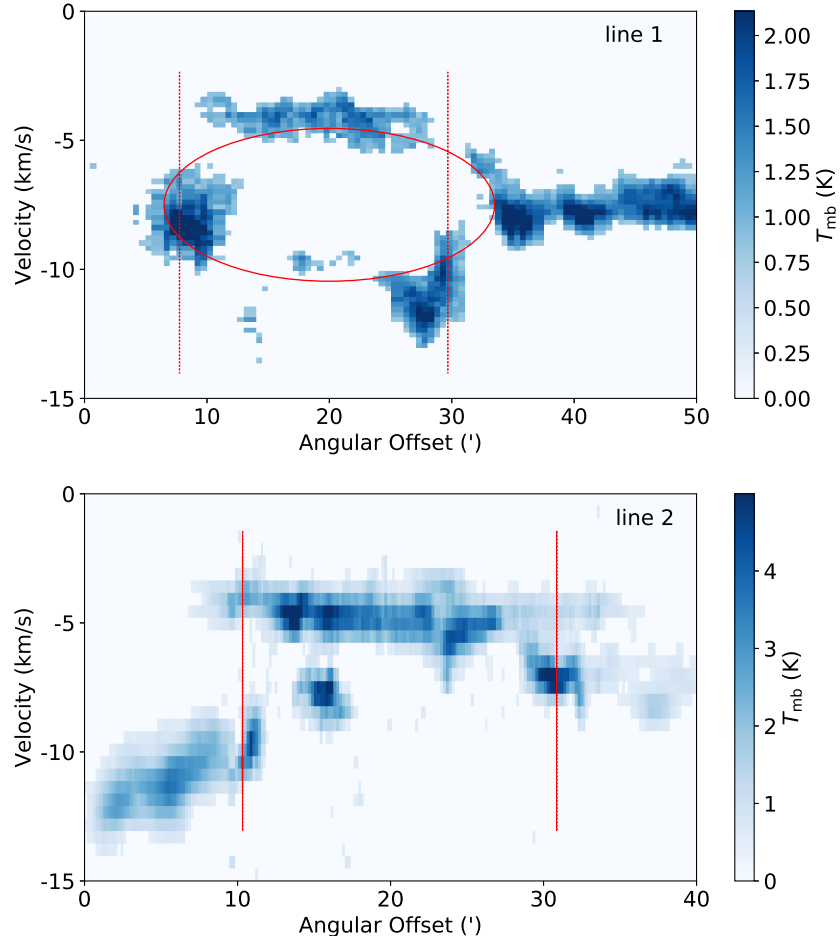


**Figure 3.** Position-velocity diagrams of  $^{12}\text{CO}$   $J=1-0$  emission for two lines that go from R.A.= $22^{\text{h}}28^{\text{m}}07^{\text{s}}.58$ , Decl.= $+60^{\circ}33'16.92''$  to R.A.= $22^{\text{h}}23^{\text{m}}54^{\text{s}}.65$ , Decl.= $+61^{\circ}12'39.6''$  with a  $52.4^{\circ}$  inclination (line1, the top panel), and from R.A.=  $22^{\text{h}}29^{\text{m}}31^{\text{s}}.56$ , Decl.= $+60^{\circ}40'46.92''$  to R.A.= $22^{\text{h}}25^{\text{m}}45^{\text{s}}.84$ , Decl.= $+61^{\circ}09'54.00''$  with a  $46.7^{\circ}$  inclination (line2, the bottom panel), respectively (see the bottom right panel of Figure 2). The red lines in each diagram delineate the edge of G106.3+2.7 (see the red small rectangles in the bottom right panel of Figure 2), and the ellipse in the top panel indicates the expanding molecular structure in the position-velocity diagram.

Kothes et al. (2001), there is a filament-like structure nicely aligning the northwestern edge of the SNR, with an orientation from the northeast to the southwest. (2) In velocity interval  $-6$  to  $-3\text{ km s}^{-1}$ , there is a ring-like structure and some diffuse  $^{12}\text{CO}$  emission toward the “belly” region (see Figure 1) of the SNR. Notably, the spatial distribution of the diffuse  $^{12}\text{CO}$  emission happens to overlap with the  $\gamma$ -ray emissions detected by Fermi-LAT (Xin et al. 2019) and the Tibet AS $\gamma$  experiment (Tibet AS $\gamma$  Collaboration 2021), while

the head/PWN part of the SNR seems faint in  $^{12}\text{CO}$  line. Actually, the LSR velocity of the MCs toward the “belly” region is very similar to that of environmental HI gas (Kothes et al. 2001).

### 3.2. Position-Velocity Diagram of the Molecular Clouds

We note some molecular structures with unusual velocity features toward the “belly” region of the SNR. Figure 3 shows the position-velocity (P-V) diagrams of slices taken along the two

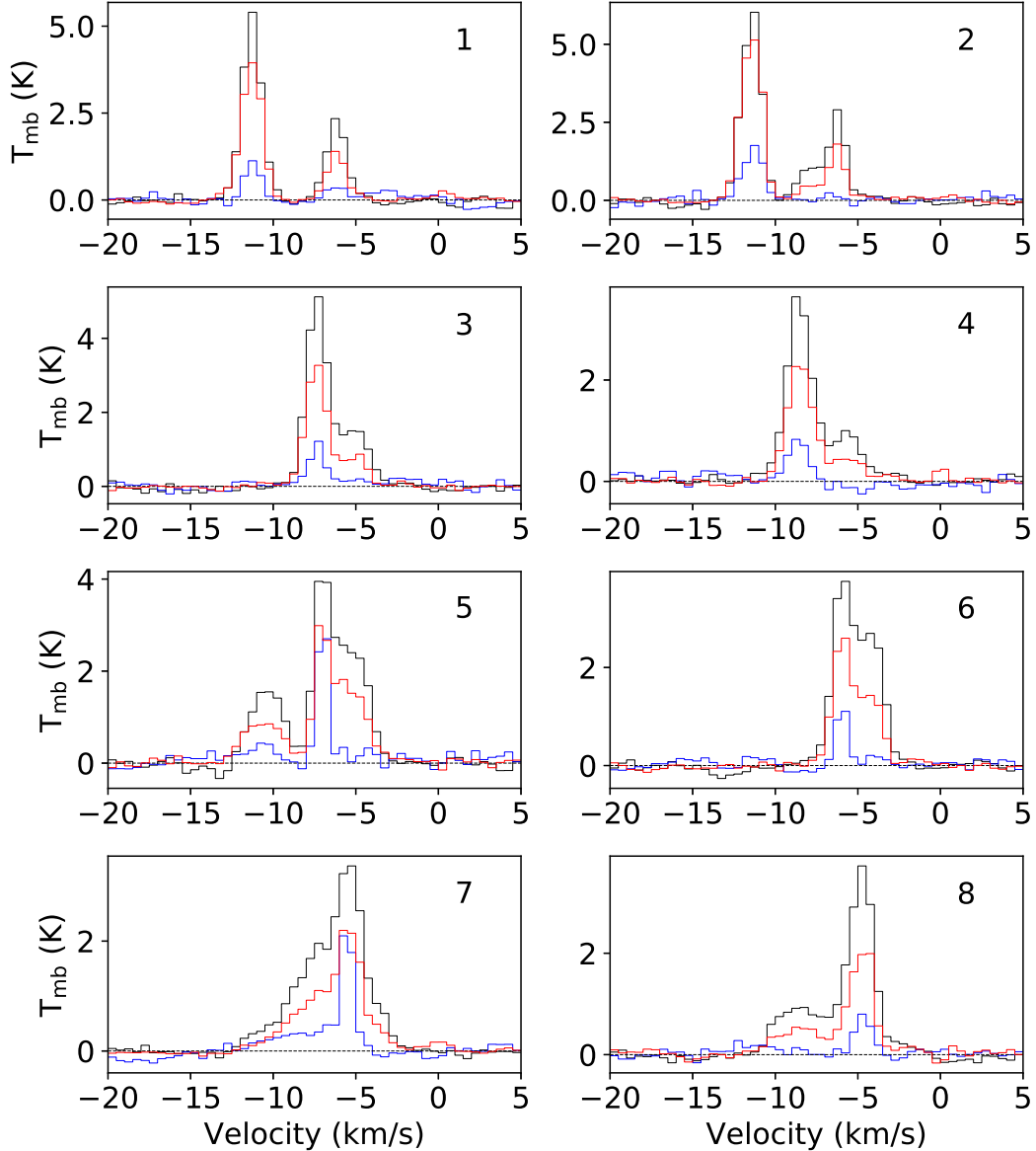


**Figure 4.** Averaged spectra of regions “1” to “8” in the velocity range  $-20$  to  $5 \text{ km s}^{-1}$ . The eight regions are defined in Figure B.4. The black lines denote the  $^{12}\text{CO } J=1-0$  spectra, the red lines denote the  $^{12}\text{CO } J=2-1$  spectra, the blue lines denote the  $^{13}\text{CO } J=1-0$  spectra, and the dashed lines represent the  $0 \text{ K}$  main-beam temperature. The  $^{13}\text{CO } J=1-0$  spectra have been multiplied by a factor of three for better visibility.

lines, labeled in the bottom right panel of Figure 2. The P-V diagram along line 1 shows an expanding molecular structure, with an angular extent larger than that of the SNR. This expanding structure is centered at  $\sim -7.5 \text{ km s}^{-1}$  with an expansion velocity of  $\sim 3.5 \text{ km s}^{-1}$  and an angular size of  $\sim 26'$ . Also, we find a velocity gradient that changes from  $\sim -3 \text{ km s}^{-1}$

at angular offset  $10'$  to  $\sim -7 \text{ km s}^{-1}$  at angular offset  $30'$  along line 2. The measured velocity variation is about  $4 \text{ km s}^{-1}$ , which is similar to the expansion velocity of the expanding structure. Because there lacks conclusive kinematic evidence of disturbance of the MCs by the shock of the SNR (see § 3.3 and 3.4), the P-V structures could be a result of other processes,

such as stellar wind(s), instead of the shock of SNR G106.3+2.7.

### 3.3. Molecular Line Profiles

The physical properties of an MC can be strongly affected if it is shocked by the SNR blast wave. Observationally, the  $^{12}\text{CO}$  line profiles can be one/two-sided broadened if the MC is located at the edge of or within the SNR, and such kinematic signatures are present in many SNR-MC interacting systems like IC 443 (e.g., White et al. 1987), W28 (e.g., Arikawa et al. 1999), Kes 75 (Su et al. 2009), 3C 397 (Jiang et al. 2010), Kes 78 (Zhou & Chen 2011), G357.7+0.3 (Rho et al. 2017), and CTB 87 (Liu et al. 2018).

To examine whether SNR G106.3+2.7 is interacting with the MCs, we have inspected the CO line profiles toward the region observed by the IRAM 30 m telescope (see Appendix A). Figure 4 shows the averaged emission line profiles delineated by the white rectangles in Figure B.4, where regions 1 to 3 are at the edge of the SNR, region 4 is outside the SNR boundary, and regions 5 to 8 are in the ‘‘belly’’ region, projectively. There are separated  $^{12}\text{CO}$  components at  $\sim -11$  and  $\sim -6 \text{ km s}^{-1}$  in both regions 1 and 2. The  $^{12}\text{CO}$  components at  $\sim -6 \text{ km s}^{-1}$  are weaker and show weaker  $^{13}\text{CO}$  line emission, which is either the red-wing broadened part of the main components at  $\sim -11 \text{ km s}^{-1}$  or a separated, irrelevant velocity component. The  $^{12}\text{CO}$  line profiles in regions 3 to 6 are similar to those in regions 1 and 2, except that the main components are at  $\sim -8 \text{ km s}^{-1}$  in regions 3 to 5 and at  $\sim -6 \text{ km s}^{-1}$  in region 6. Further, there is a weak peak at  $\sim -11 \text{ km s}^{-1}$  in region 5. There are main  $^{12}\text{CO}$  components at  $\sim -5 \text{ km s}^{-1}$  in both regions 7 and 8, while there seem to be blue-wing broadened parts at  $\sim -11$  to  $-7 \text{ km s}^{-1}$ . We note that the profiles of the  $^{12}\text{CO}$  lines are systematically asymmetric in the ‘‘belly’’ region of the SNR (regions 1–3 and 5–8). However, there are similar  $^{12}\text{CO}$  line

profiles in the region outside the SNR boundary (region 4). Furthermore, the widths of the asymmetric wings are only a few  $\text{km s}^{-1}$ , indicating that the disturbance in the molecular gas is not strong. Therefore, it is uncertain whether the broadened profiles in the region projected inside the SNR are the results of interaction between the SNR shock and the MC. Alternatively, they could be a signature of other perturbed processes, such as perturbation by the stellar wind(s).

### 3.4. The $^{12}\text{CO } J=2-1/J=1-0$ Line Ratio

The  $^{12}\text{CO } J=2-1/J=1-0$  line ratios ( $R_{21/10}$ ) at the CO line wings could be enhanced ( $\gtrsim 1$ ) if the molecular gas is disturbed and heated by the SNR shock (e.g., Seta et al. 1998; Jiang et al. 2010; Sano et al. 2019, 2020). By inspecting the spectral properties of the CO emissions, we have not found enhanced  $^{12}\text{CO } J=2-1/J=1-0$  line ratios at the CO line wings toward the region observed with IRAM 30 m telescope (see Figures 4, A.1, A.2, and A.3).

Figure 5 shows the spatial distribution of the ratio  $R_{21/10}$  of the molecular gas in velocity intervals  $-15$  to  $-9 \text{ km s}^{-1}$  and  $-9$  to  $-1 \text{ km s}^{-1}$ . We do not show the pixels where the values are smaller than  $5\sigma$  for either  $^{12}\text{CO } J=2-1$  or  $^{12}\text{CO } J=1-0$  emission. Although the  $^{12}\text{CO } J=2-1/J=1-0$  line ratios in some pixels just outside the northern edge of the SNR could reach unity in velocity interval  $-15$  to  $-9 \text{ km s}^{-1}$ , they mainly arise from the CO line centers instead of the line wings (see Figure A.1). This means that this MC with high  $R_{21/10}$  has a relatively higher kinetic temperature (see Appendix B) but is not shocked and is a quiescent MC outside the SNR. On the other hand, the line ratios in all other pixels are clearly smaller than unity.

## 4. DISCUSSION

SNR G106.3+2.7 has been found to be a  $\gamma$ -ray emitting source in the band from GeV to sub-PeV (e.g., Xin et al. 2019; Albert et al.

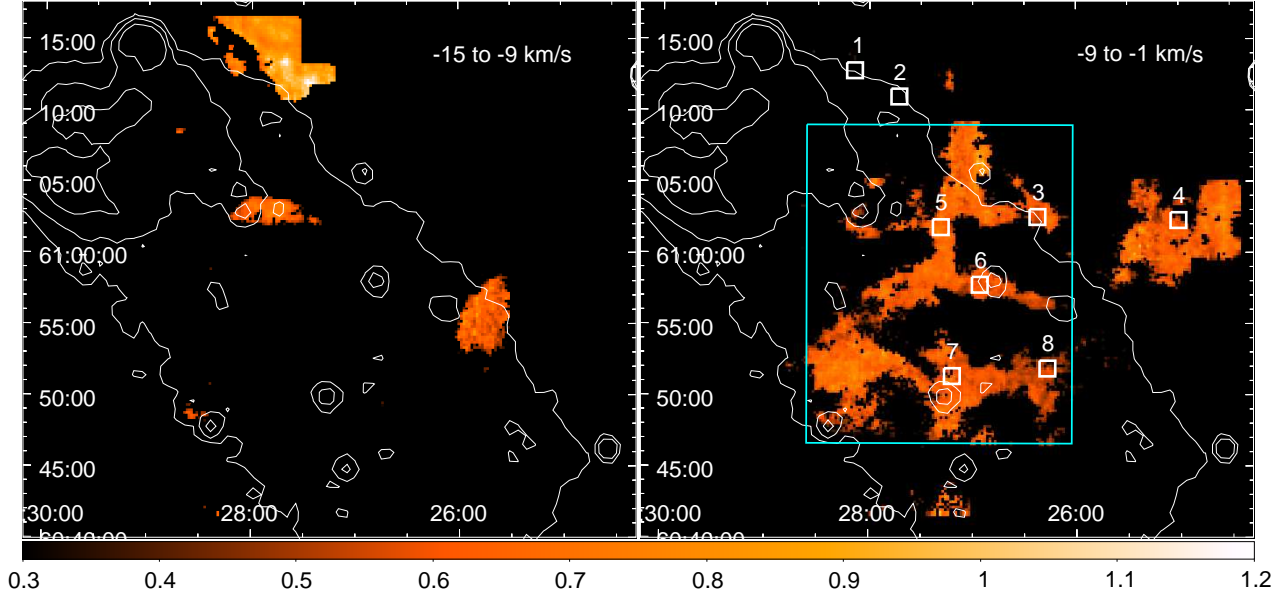


**Figure 5.** Ratio maps of IRAM  $^{12}\text{CO } J=2-1/J=1-0$  for LSR velocity ranges  $-15$  to  $-9 \text{ km s}^{-1}$  (left panel) and  $-9$  to  $-1 \text{ km s}^{-1}$ . The pixels toward which the value are smaller than  $5\sigma$  for either  $^{12}\text{CO } J=2-1$  or  $^{12}\text{CO } J=1-0$  have been omitted. The regions delineated by white rectangles are used to extract CO spectra (Figure 4), and the region delineated by the cyan rectangle is used to estimate the properties of the MC toward the “belly” region of G106.3+2.7 in velocity range  $-9$  to  $-1 \text{ km s}^{-1}$  (Section 4). The radio contours are the same as those in Figure 1.

2020; Tibet AS $\gamma$  Collaboration 2021; Cao et al. 2021). The main part of the  $\gamma$ -ray emission appears to be spatially correspondent with the CO emission in LSR velocity interval  $-6$  to  $-3 \text{ km s}^{-1}$  projected in the “belly” region of the SNR (e.g., Xin et al. 2019; Tibet AS $\gamma$  Collaboration 2021). By parameterizing the distance to the MC as  $d_{0.8} = d/(0.8 \text{ kpc})$  (Kothes et al. 2001), the mass of the molecular gas in velocity range  $-9$  to  $-1 \text{ km s}^{-1}$  within the cyan rectangle region delineated in Figure 5 is estimated to be about  $330d_{0.8}M_{\odot}$  and  $860d_{0.8}M_{\odot}$  from  $^{13}\text{CO}$  and  $^{12}\text{CO}$  emissions<sup>2</sup> respectively (see Appendix C). Assuming the length of the cloud along the line of sight (LOS) is comparable to its projected size ( $\sim 4.8 \text{ pc}$ ), the molecular density of the cloud is estimated to be about

<sup>2</sup> The mass of the MC estimated using  $^{12}\text{CO}$  here could have large uncertainty, as the X-factor method is more reliable for MC with a mass of order larger than  $10^4 M_{\odot}$  (Bolatto et al. 2013).

$30 \text{ cm}^{-3}$  and  $80 \text{ cm}^{-3}$ , respectively. Our observation also shows that a filament follows the northern radio boundary of the SNR in velocity interval  $-8$  to  $-5 \text{ km s}^{-1}$ . Asymmetrical  $^{12}\text{CO}$  line profiles are found in some locations along the northern boundary and in the “belly” region of G106.3+2.7, but we could not conclude that they represent the kinematic evidence of shock-MC interaction since we also see similar  $^{12}\text{CO}$  line profiles outside the SNR (Figure 4). Physical signature of interaction (such as elevated gas temperature or  $^{12}\text{CO } J=2-1/J=1-0$  line ratio) has not been found either along the filament or in the MC toward the “belly” of the SNR (Figures B.4 and 5). Nonetheless, we can not exclude the possible proximity of the MC to the SNR along the LOS. In such a scenario, the accelerated protons that escape from the SNR shock can illuminate the MC via p-p hadronic interaction.

Except for SNR(s), other possible Galactic CR accelerators, such as cluster(s) with massive stars (e.g., Aharonian et al. 2019; Morlino et al. 2021), are also worth considering. We note that there are structural properties in the MCs toward the gamma-ray emitting region in the velocity range of about  $-11$  to  $-3 \text{ km s}^{-1}$  (see § 3.1 and 3.2). Especially, an expanding molecular structure and a velocity gradient across the “belly” region of G106.3+2.7 in the P-V diagram (§ 3.2) might be the results of massive stellar winds. The radius  $R$  and the expansion velocity  $v$  of the expanding structure are about  $12'$  (corresponding to  $\sim 2.9d_{0.8} \text{ pc}$ ) and  $3.5 \text{ km s}^{-1}$ , respectively (§ 3.2). If it is blown by the interior stellar wind(s), its age could be estimated to be (Weaver et al. 1977)  $t = 3R/5v = 5 \times 10^5 d_{0.8} (v/3.5 \text{ km s}^{-1})^{-1} \text{ yr}$ . Furthermore, the kinetic luminosity of the stellar wind(s) could be (Weaver et al. 1977):  $L_w \sim 1.2 \times 10^{34} (n/100 \text{ cm}^{-3}) (v/3.5 \text{ km s}^{-1})^3 d_{0.8}^2 \text{ erg s}^{-1}$ , where  $n$  is the atomic hydrogen number density of the molecular gas. The estimated luminosity of the stellar wind(s) is typical for an O9V to B0V type star (e.g., Elson et al. 1989; Chen et al. 2013). We have searched for massive star(s) using the *Tycho-2* Spectral Type Catalog (Wright et al. 2003) toward this region, yet no OB star cluster/association or massive main sequence star has been found, and it is unlikely to be a result of incompleteness of the catalog we use (see Appendix D). Therefore, we suggest that the expanding structure and the velocity gradient of the molecular gas could be due to the progenitor wind of G106.3+2.7. We note that similar structures due to progenitor winds have also been found in a few other SNRs, such as Tycho (Zhou et al. 2016; Chen et al. 2017), N132D (Sano et al. 2020), and VRO 42.05.01 (Arias et al. 2019).

## 5. SUMMARY

We have investigated the molecular environment of G106.3+2.7 using the CO-line data obtained with the IRAM 30 m telescope toward the “belly” region of the SNR, which is coincident with the centroid region of the  $\gamma$ -ray emission. There is a filament that follows the north radio boundary of the SNR in velocity interval  $-8$  to  $-5 \text{ km s}^{-1}$ . Some asymmetric broad profiles of  $^{12}\text{CO}$  lines are found not only toward the “belly” region of the SNR but also outside the boundary. Further, the  $^{12}\text{CO } J=2-1/J=1-0$  line ratios of the MCs are similar to the typical value for interstellar MCs. Therefore, it is uncertain about whether the MCs are disturbed by the SNR shock. Nonetheless, we can not exclude the possible proximity of the MC to the SNR along the LOS, which facilitates illumination of the MC by the accelerated protons that escape from the SNR shock via p-p hadronic interaction. Notably, we find an expanding molecular structure and a velocity gradient toward the “belly” region of the SNR, and we propose a possibility of their relations to the progenitor wind of the SNR.

We are grateful to Xiao Zhang for the discussion about the gamma-ray emission toward this SNR, Xin Zhou for the discussion about the methods to estimate the properties of the MCs, Niu Liu and Yong Shao for a discussion about how to search for OB stars in the field of view. We thank the staff of the IRAM 30 m observatory for the help during the remote observation. This work is supported by the National Key R&D Program of China under grants 2017YFA0402600, and the NSFC under grants 11773014, 11633007, 11503008, and 11590781. Q.C.L. acknowledges support from the program A for Outstanding PhD candidate of Nanjing University.

## REFERENCES

- Abdo, A. A., Allen, B., Berley, D., et al. 2007, *ApJL*, 664, L91, doi: [10.1086/520717](https://doi.org/10.1086/520717)
- Abdo, A. A., Ackermann, M., Ajello, M., et al. 2009, *ApJ*, 706, 1331, doi: [10.1088/0004-637X/706/2/1331](https://doi.org/10.1088/0004-637X/706/2/1331)
- Acciari, V. A., Aliu, E., Arlen, T., et al. 2009, *ApJL*, 703, L6, doi: [10.1088/0004-637X/703/1/L6](https://doi.org/10.1088/0004-637X/703/1/L6)
- Aharonian, F., Yang, R., & de Oña Wilhelmi, E. 2019, *Nature Astronomy*, 3, 561, doi: [10.1038/s41550-019-0724-0](https://doi.org/10.1038/s41550-019-0724-0)
- Albert, A., Alfaro, R., Alvarez, C., et al. 2020, *ApJL*, 896, L29, doi: [10.3847/2041-8213/ab96cc](https://doi.org/10.3847/2041-8213/ab96cc)
- Arias, M., Domček, V., Zhou, P., & Vink, J. 2019, *A&A*, 627, A75, doi: [10.1051/0004-6361/201935528](https://doi.org/10.1051/0004-6361/201935528)
- Arikawa, Y., Tatematsu, K., Sekimoto, Y., & Takahashi, T. 1999, *PASJ*, 51, L7, doi: [10.1093/pasj/51.4.L7](https://doi.org/10.1093/pasj/51.4.L7)
- Bao, Y., & Chen, Y. 2021, *ApJ*, in press, arXiv:2103.01814. <https://arxiv.org/abs/2103.01814>
- Bolatto, A. D., Wolfire, M., & Leroy, A. K. 2013, *ARA&A*, 51, 207, doi: [10.1146/annurev-astro-082812-140944](https://doi.org/10.1146/annurev-astro-082812-140944)
- Cao, Z., Aharonian, F. A., An, Q., et al. 2021, *Nature*, 594, 33, doi: [10.1038/s41586-021-03498-z](https://doi.org/10.1038/s41586-021-03498-z)
- Chen, X., Xiong, F., & Yang, J. 2017, *A&A*, 604, A13, doi: [10.1051/0004-6361/201630003](https://doi.org/10.1051/0004-6361/201630003)
- Chen, Y., Jiang, B., Zhou, P., et al. 2014, in *Supernova Environmental Impacts*, ed. A. Ray & R. A. McCray, Vol. 296, 170–177, doi: [10.1017/S1743921313009423](https://doi.org/10.1017/S1743921313009423)
- Chen, Y., Zhou, P., & Chu, Y.-H. 2013, *ApJL*, 769, L16, doi: [10.1088/2041-8205/769/1/L16](https://doi.org/10.1088/2041-8205/769/1/L16)
- Dame, T. M., Hartmann, D., & Thaddeus, P. 2001, *ApJ*, 547, 792, doi: [10.1086/318388](https://doi.org/10.1086/318388)
- Elson, R. A. W., Fall, S. M., & Freeman, K. C. 1989, *ApJ*, 336, 734, doi: [10.1086/167046](https://doi.org/10.1086/167046)
- Foight, D. R., Güver, T., Özel, F., & Slane, P. O. 2016, *ApJ*, 826, 66, doi: [10.3847/0004-637X/826/1/66](https://doi.org/10.3847/0004-637X/826/1/66)
- Frerking, M. A., Langer, W. D., & Wilson, R. W. 1982, *ApJ*, 262, 590, doi: [10.1086/160451](https://doi.org/10.1086/160451)
- Fujita, Y., Bamba, A., Nobukawa, K. K., & Matsumoto, H. 2021, arXiv e-prints, arXiv:2101.10329. <https://arxiv.org/abs/2101.10329>
- Ge, C., Liu, R.-Y., Niu, S., Chen, Y., & Wang, X.-Y. 2021, *The Innovation*, 2, 100118, doi: [10.1016/j.xinn.2021.100118](https://doi.org/10.1016/j.xinn.2021.100118)
- Halpern, J. P., Camilo, F., Gotthelf, E. V., et al. 2001a, *ApJL*, 552, L125, doi: [10.1086/320347](https://doi.org/10.1086/320347)
- Halpern, J. P., Gotthelf, E. V., Leighly, K. M., & Helfand, D. J. 2001b, *ApJ*, 547, 323, doi: [10.1086/318361](https://doi.org/10.1086/318361)
- Høg, E., Fabricius, C., Makarov, V. V., et al. 2000, *A&A*, 355, L27
- Jiang, B., Chen, Y., Wang, J., et al. 2010, *ApJ*, 712, 1147, doi: [10.1088/0004-637X/712/2/1147](https://doi.org/10.1088/0004-637X/712/2/1147)
- Kothes, R., Uyaniker, B., & Pineault, S. 2001, *ApJ*, 560, 236, doi: [10.1086/322511](https://doi.org/10.1086/322511)
- Liu, Q.-C., Chen, Y., Chen, B.-Q., et al. 2018, *ApJ*, 859, 173, doi: [10.3847/1538-4357/aabfe1](https://doi.org/10.3847/1538-4357/aabfe1)
- Liu, Q.-C., Chen, Y., Zhou, P., Zhang, X., & Jiang, B. 2020a, *ApJ*, 892, 143, doi: [10.3847/1538-4357/ab7a22](https://doi.org/10.3847/1538-4357/ab7a22)
- Liu, S., Zeng, H., Xin, Y., & Zhu, H. 2020b, *ApJL*, 897, L34, doi: [10.3847/2041-8213/ab9ff2](https://doi.org/10.3847/2041-8213/ab9ff2)
- Morlino, G., Blasi, P., Peretti, E., & Cristofari, P. 2021, arXiv e-prints, arXiv:2102.09217. <https://arxiv.org/abs/2102.09217>
- Pineault, S., & Joncas, G. 2000, *AJ*, 120, 3218, doi: [10.1086/316863](https://doi.org/10.1086/316863)
- Rho, J., Hewitt, J. W., Bieging, J., et al. 2017, *ApJ*, 834, 12, doi: [10.3847/1538-4357/834/1/12](https://doi.org/10.3847/1538-4357/834/1/12)
- Sano, H., Matsumura, H., Yamane, Y., et al. 2019, *ApJ*, 881, 85, doi: [10.3847/1538-4357/ab2ade](https://doi.org/10.3847/1538-4357/ab2ade)
- Sano, H., Plucinsky, P. P., Bamba, A., et al. 2020, *ApJ*, 902, 53, doi: [10.3847/1538-4357/abb469](https://doi.org/10.3847/1538-4357/abb469)
- Seta, M., Hasegawa, T., Dame, T. M., et al. 1998, *ApJ*, 505, 286, doi: [10.1086/306141](https://doi.org/10.1086/306141)
- Su, Y., Chen, Y., Yang, J., et al. 2009, *ApJ*, 694, 376, doi: [10.1088/0004-637X/694/1/376](https://doi.org/10.1088/0004-637X/694/1/376)
- Taylor, A. R., Gibson, S. J., Peracaula, M., et al. 2003, *AJ*, 125, 3145, doi: [10.1086/375301](https://doi.org/10.1086/375301)
- Tibet AS $\gamma$  Collaboration. 2021, *Nature Astronomy*, 5, 460, doi: [10.1038/s41550-020-01294-9](https://doi.org/10.1038/s41550-020-01294-9)
- Weaver, R., McCray, R., Castor, J., Shapiro, P., & Moore, R. 1977, *ApJ*, 218, 377, doi: [10.1086/155692](https://doi.org/10.1086/155692)
- Wegner, W. 2006, *MNRAS*, 371, 185, doi: [10.1111/j.1365-2966.2006.10549.x](https://doi.org/10.1111/j.1365-2966.2006.10549.x)
- White, G. J., Rainey, R., Hayashi, S. S., & Kaifu, N. 1987, *A&A*, 173, 337

Wright, C. O., Egan, M. P., Kraemer, K. E., &

Price, S. D. 2003, *AJ*, 125, 359,

doi: [10.1086/345511](https://doi.org/10.1086/345511)

Xin, Y., Zeng, H., Liu, S., Fan, Y., & Wei, D.  
2019, *ApJ*, 885, 162,

doi: [10.3847/1538-4357/ab48ee](https://doi.org/10.3847/1538-4357/ab48ee)

Zhou, P., & Chen, Y. 2011, *ApJ*, 743, 4,

doi: [10.1088/0004-637X/743/1/4](https://doi.org/10.1088/0004-637X/743/1/4)

Zhou, P., Chen, Y., Zhang, Z.-Y., et al. 2016,

*ApJ*, 826, 34, doi: [10.3847/0004-637X/826/1/34](https://doi.org/10.3847/0004-637X/826/1/34)

## APPENDIX

## A. GRID OF THE CO SPECTRA OBSERVED BY THE IRAM 30 M TELESCOPE

We have inspected the CO line profiles toward the SNR G106.3+2.7 region observed by the IRAM 30 m telescope. Because the pixel sizes of the original datacubes are too small ( $11''$ ), we have re-gridded the datacubes to reach pixel sizes of  $66''$  before making the grids of  $^{12}\text{CO } J=1-0$ ,  $^{12}\text{CO } J=2-1$ , and  $^{13}\text{CO } J=1-0$  spectra. Figures A.1, A.2, and A.3 show the grids of CO spectra in velocity range  $-15$  to  $+5 \text{ km s}^{-1}$  for the regions delineated by the white rectangles labeled with “N”, “S”, and “W” in the right panel of Figure 5, respectively. There are many pixels, either within, on, or outside the boundary of the SNR G106.3+2.7, where the profiles of  $^{12}\text{CO}$  spectra seemingly to be asymmetric broadened. The averaged CO line profiles of some of the pixels (regions “1” to “8” marked in Figures B.4 and 5) are studied in detail in Section 3.3.

## B. TEMPERATURE DISTRIBUTION OF THE MOLECULAR CLOUDS

The kinetic temperature of the molecular gas ( $T_k$ ), which is approximately equal to the excitation temperature ( $T_{\text{ex}}$ ) under the assumption of local thermodynamic equilibrium, can be estimated from the peak of the main-beam temperature  $T_{\text{mb}}$  of the  $^{12}\text{CO } J=1-0$  line emission with equation  $T_k = 5.53/\{\ln[1+5.53/(T_{\text{mb}}+0.84)]\}$  K, where the beam filling factor is assumed to be equal to 1. Figure B.4 shows the spatial distribution of the kinetic temperature of the molecular gas in velocity intervals  $-15$  to  $-9 \text{ km s}^{-1}$  and  $-9$  to  $-1 \text{ km s}^{-1}$ , corresponding to the velocity ranges of the two components shown in the top left panel of Figure 2. The kinetic temperature in each pixel is estimated from the peak of the main-beam temperature in the given velocity range. The kinetic temperatures are  $\lesssim 10$  K for the most part of the molecular gas in both velocity ranges, except for the clump at the northern corner in velocity interval  $-15$  to  $-9 \text{ km s}^{-1}$ . That is, the distribution of the kinetic temperature is similar to that of the  $^{12}\text{CO } J=2-1/J=1-0$  line ratios. Actually, the higher line ratio toward the northern corner in this velocity interval could be directly related to the higher kinetic temperature there (see, e.g., Liu et al. 2020a).

## C. THE MASS OF THE MOLECULAR CLOUD TOWARD THE “BELLY” OF G106.3+2.7

The mass of the molecular gas in velocity range  $-9$  to  $-1 \text{ km s}^{-1}$  toward the “belly” of G106.3+2.7 could be roughly estimated from the column density of the MC in the given region. The angular size of the region delineated by the cyan rectangle in the right panel of Figure 5 is  $\sim 18'.5 \times 22'.5$ , which can be translated to a physical size of  $\sim 4.3d_{0.8} \text{ pc} \times 5.2d_{0.8} \text{ pc}$ . The column density of  $\text{H}_2$  within this region is estimated from either  $^{13}\text{CO } J=1-0$  or  $^{12}\text{CO } J=1-0$  line. When assuming the molecular gas to be in local thermodynamic equilibrium and the  $^{12}\text{CO } J=1-0$  line to be optically thick, the column density could be estimated using  $N(\text{H}_2) \approx 7 \times 10^5 N(^{13}\text{CO})$  (Frerking et al. 1982). Here  $N(^{13}\text{CO}) = 2.42 \times 10^{14} \int T_{\text{mb}}(^{13}\text{CO}) dv / (1 - \exp(-5.3/T_{\text{ex}})) \text{ cm}^{-2}$  is the column density of  $^{13}\text{CO}$ . On the other hand, it could also be estimated using the CO-to- $\text{H}_2$  mass conversion factor ( $N(\text{H}_2)/W(^{12}\text{CO})$ ; the “X-factor”), which is assumed to be  $1.8 \times 10^{20} \text{ cm}^{-2} \text{ K}^{-1} \text{ km}^{-1} \text{ s}$  (Dame et al. 2001). The mass of this MC is thus estimated to be about  $330d_{0.8}M_\odot$  and  $860d_{0.8}M_\odot$  from  $^{13}\text{CO}$  and  $^{12}\text{CO}$  lines, respectively.

## D. THE MASSIVE STARS TOWARD G106.3+2.7

We use the *Tycho-2* Spectral Type Catalog (Wright et al. 2003), which is about 90% complete at an apparent visual magnitude of  $\sim 11.5$  (Høg et al. 2000), to search for massive stars that can

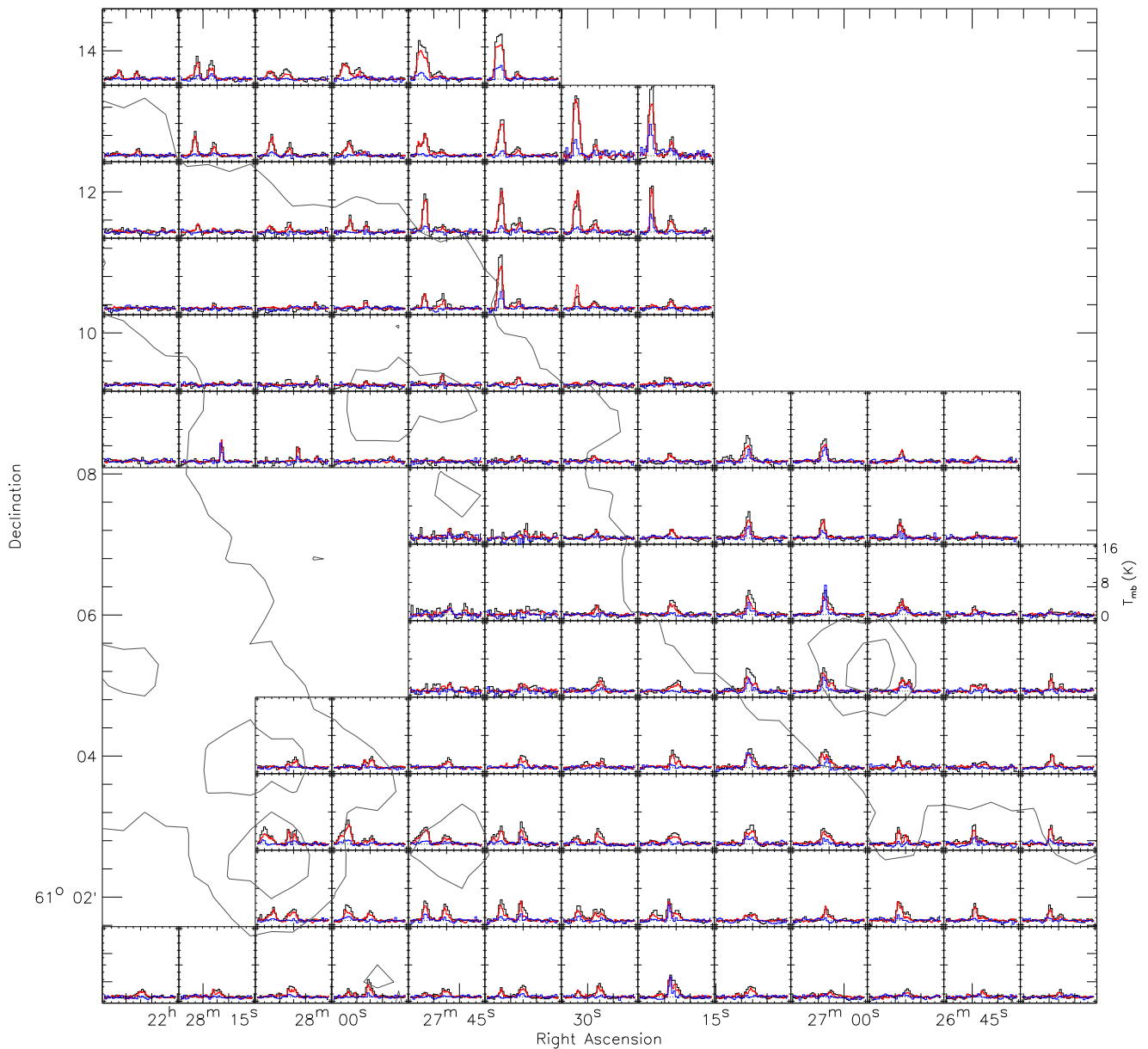


**Figure A.1.** Grid of  $^{12}\text{CO } J=1-0$ ,  $^{12}\text{CO } J=2-1$ , and  $^{13}\text{CO } J=1-0$  spectra observed by the IRAM 30 m telescope in velocity range  $-15$  to  $+5 \text{ km s}^{-1}$  for the region delineated by the white rectangle labeled with “N” in the right panel of Figure B.4. The black lines denote the  $^{12}\text{CO } J=1-0$  spectra, the red lines denote the  $^{12}\text{CO } J=2-1$  spectra, and the blue lines denote the  $^{13}\text{CO } J=1-0$  spectra. The  $^{13}\text{CO } J=1-0$  spectra have been multiplied by a factor of two for better visibility. The size of each pixel is  $66'' \times 66''$ . The contours are the same as those in Figure 1.

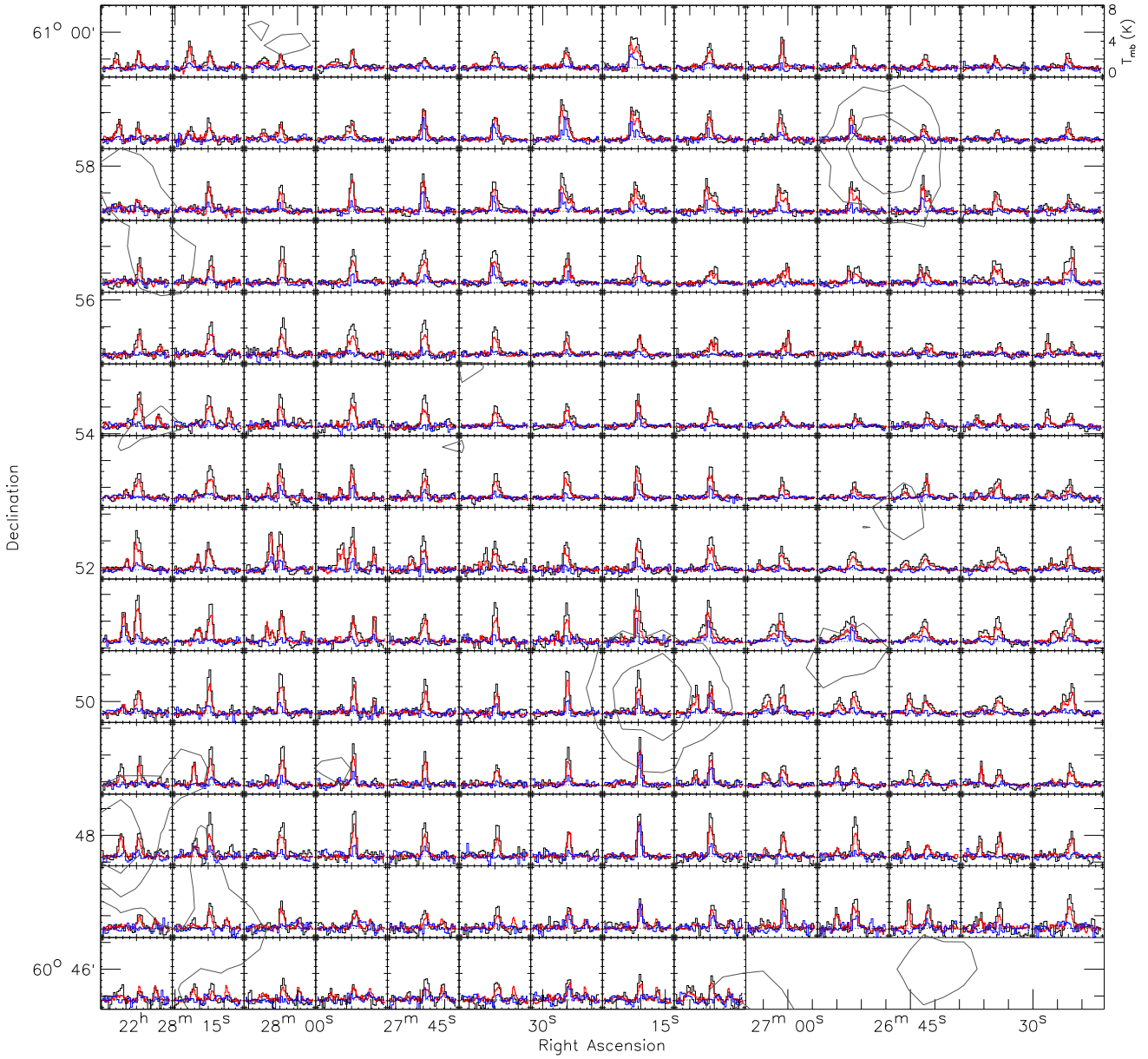


**Figure A.2.** The same as Figure A.1, but for the region delineated by the white rectangle labeled with “S” in the right panel of Figure B.4. The  $^{13}\text{CO } J=1-0$  spectra also have been multiplied by a factor of two for better visibility.

potentially produce wind-blown structure (O–B3V star; e.g., [Chen et al. 2013](#)) toward G106.3+2.7 in a circular region centered at R.A.=22<sup>h</sup>27<sup>m</sup>12<sup>s</sup>.58, decl.=+60°46′19.9″, 30′ in radius. However, no massive star has been found toward G106.3+2.7, which is unlikely to be a result of optical extinction. The optical extinction can be estimated from the empirical relation  $N_{\text{H}} = (2.87 \pm 0.12) \times 10^{21} A_V \text{ cm}^{-2}$  ([Foight et al. 2016](#)), where  $N_{\text{H}} = 2N(\text{H}_2) + N_{\text{HI}}$  ( $\sim 9.5 \times 10^{21} \text{ cm}^{-2}$ , [Ge et al. 2021](#)) is the foreground

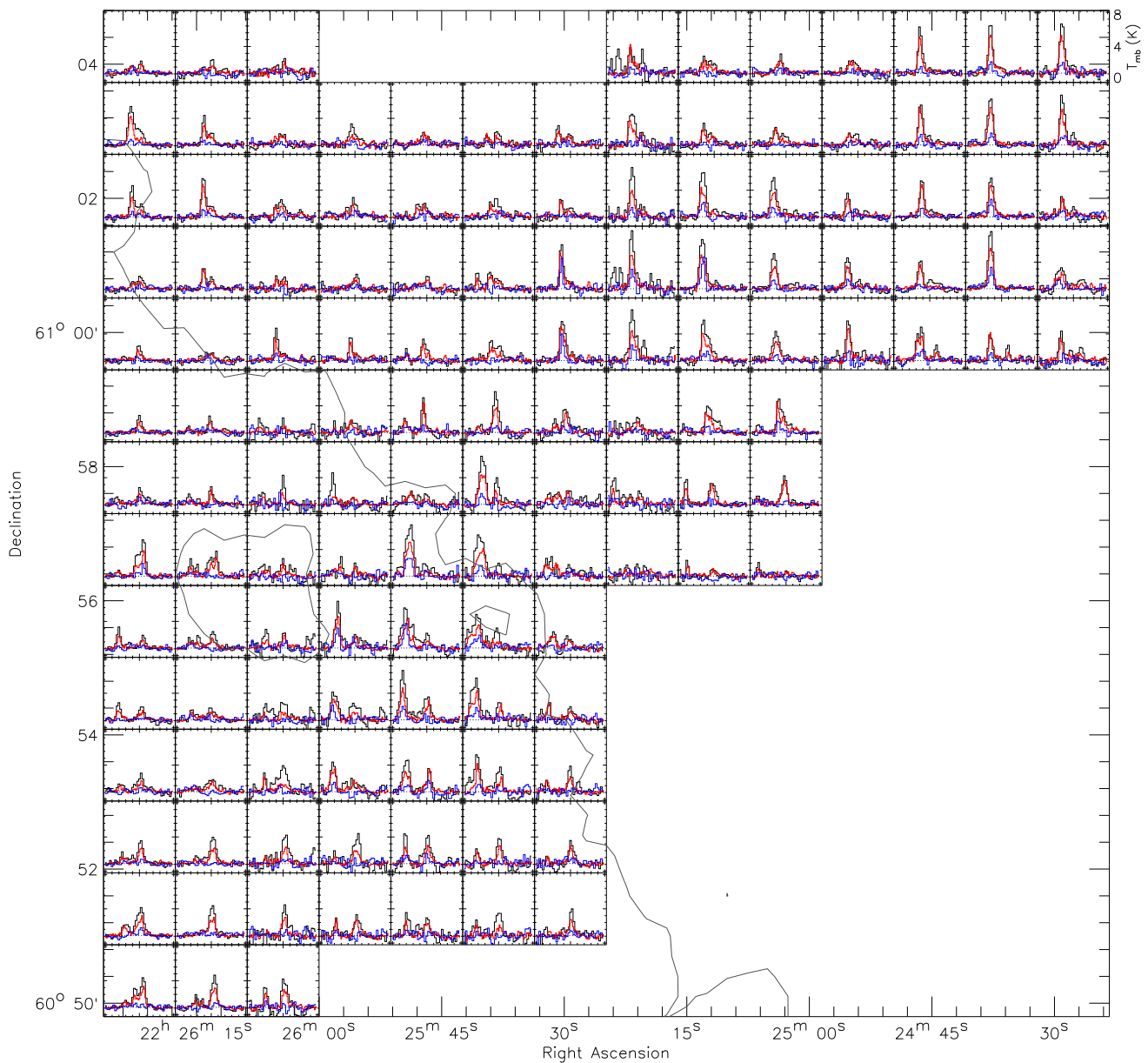


**Figure A.3.** The same as Figure A.1, but for the region delineated by the white rectangle labeled with “W” in the right panel of Figure B.4. The  $^{13}\text{CO}$   $J=1-0$  spectra also have been multiplied by a factor of two for better visibility.

hydrogen (including atoms and molecules) column density. Therefore, the optical extinction can be estimated to be  $A_V = 3.31 \pm 0.15$ . According to the relation  $V = M_V - 5 + 5 \log D + A_V$ , where  $V$  is the apparent visual magnitude,  $M_V$  is the absolute magnitude ( $\leq -1.68$  for stars earlier than B3V type; e.g., Wegner 2006),  $D$  is the distance to the star in units of pc, the apparent visual magnitude

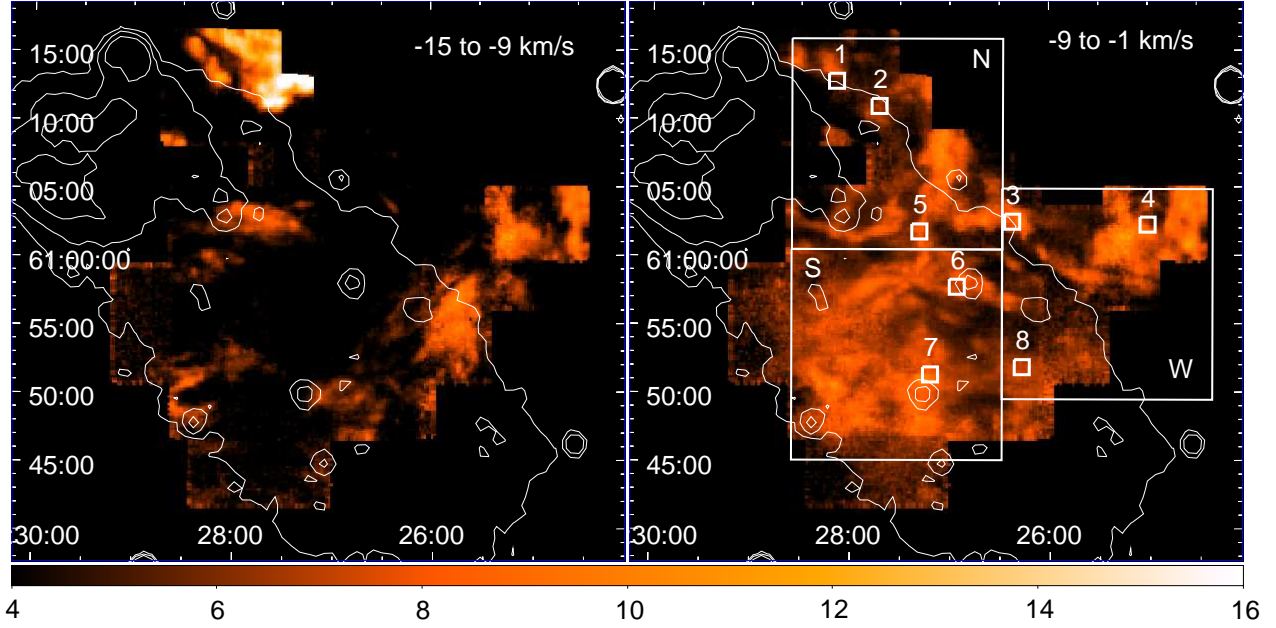


**Figure B.4.** Kinetic temperature ( $T_k$ ) maps of the MCs in velocity intervals  $-15$  to  $-9 \text{ km s}^{-1}$  (left panel) and  $-9$  to  $-1 \text{ km s}^{-1}$  (right panel) obtained from the IRAM 30 m telescope observation, with the assumptions of no beam dilution ( $f = 1$ ) and  $\tau_{12CO} \gg 1$ . The contours are the same as in Figure 1. The three regions delineated by large white rectangles and labeled with “N”, “S”, and “W” are used to extract the CO grid spectra (Figure A.1, A.2, and A.3). The regions delineated by small white rectangles are the same as those in Figure 5.

of a massive star at the distance of G106.3+2.7 (about 800 pc; Kothés et al. 2001)  $\leq 11.1$ , which should have been smaller than 11.5.